Microelectronic Engineering 91 (2012) 1–8

Contents lists available at SciVerse ScienceDirect

Microelectronic Engineering

journal homepage: www.elsevier.com/locate/mee

Multi-variable thermal design of T-structured phase-change memory cell using advanced response surface method

Sangwoo Shin, Beom Seok Kim, Kyung Min Kim, Hyung Hee Cho *

Department of Mechanical Engineering, Yonsei University, Seoul 120-749, Republic of Korea

ARTICLE INFO

Article history:
Received 31 March 2011
Received in revised form 14 November 2011
Accepted 15 November 2011
Available online 23 November 2011

Keywords:
Phase-change memory device
Thermal design
Advanced response surface method

ABSTRACT

Thermal design is crucial in designing phase-change memory (PCM) as it is operated by thermal energy. Among the numerous factors that influence the performance of PCM, geometrical configuration is the most critical factor as the heat confinement is determined by the effective thermal resistance of the PCM cell. This study reports the thermal design of T-structured PCM cell with contact diameter of 80 nm. Five design variables, which are the thicknesses of two metal contact layers, two metal electrode layers, and one phase-change layer, are studied. Cell performance is evaluated in terms of the highest cell temperature during the reset process. The performance results of the five variables are correlated into a single equation using the advanced response surface method, which is a modified form of conventional response surface method. By doing this, one can easily design and define the PCM with the best performance under given constraints. Given design ranges, results show that the cell performance is maximum when the two top metal layers and the bottom metal electrode become thinner while the bottom metal contact becomes thicker. However, there exists a certain phase-change layer thickness, which is 36 nm in this study, for the maximum performance to occur.

© 2011 Elsevier B.V. All rights reserved.

1. Introduction

During the last decade, considerable degree of research on the next-generation nonvolatile memory has been made as the technological barriers of the conventional memory devices are emerging, i.e. limited feature dimension, volatility, low read/write speed, complexness, unreliability, high power consumption, etc. [1]. Among numerous candidates for the next-generation nonvolatile memory device, the phase-change memory (PCM) device has received prominent interest in recent due to its non-volatility, fast speed, low power consumption, scalability, simplicity, reliability, retentivity, etc. [1–5].

PCM is operated based on the reversible phase-change process of the chalcogenide material between the amorphous and the (poly)crystalline state. Phase-change is mediated by localized Joule heating, which is solely a transient heat conduction phenomenon. In temporal scale of tens of nanoseconds, the temperature inside the phase-change layer must reach up to $\sim$900 K to change its phase and to operate properly. Therefore, effective heat captivation is essential in enhancing the performance of the device and such temperature rise time can be a direct measure of the device performance. Many factors influence the temperature evolution behavior inside PCM such as material properties, geometrical configurations, and input power. Considering fabrication and engineering feasibility issues, geometrical configuration can be regarded as the major factor contributing to the device temperature.

To accommodate efficient heat captivation by changing the geometries, several types of PCM devices have been developed from the beginning of the PCM research to the most recent, e.g., T-structured [6–9], I-structured [4–7,10–12], line-type [1], etc. The well-known T-structured PCM cell consists of a narrow cylindrical electrode connected to the bottom of the phase-change layer (see Fig. 1). Localized Joule heating occurs adjacent to the edge of T-junction as the current is mostly concentrated in such region while expanding towards the top electrode. Temperature evolution due to the localized Joule heating is mainly influenced by the geometrical feature size, i.e. thickness of the constituting layers as they directly determine the total effective thermal resistance of the cell. Moreover, the thicknesses of the constituting layers strongly influence each other on the heat transfer behavior. Therefore, it is evident that one should definitely consider all the geometrical factors simultaneously when designing and analyzing PCM.

Previously, numerous studies regarding thermal behavior of PCM for enhancing its performance have been reported [1,4–7]. While there have been few reports on cell optimization of PCM [11–13], to the best of the authors' knowledge, no systematic thermal design and optimization regarding multi-geometrical features with the use of a proper correlation method have been yet conducted. As explained, this is important when designing the

* Corresponding author. Tel.: +82 2 2123 2828; fax: +82 2 312 2159.
E-mail address: hhcho@yonsei.ac.kr (H.H. Cho).

0167-9317/$ - see front matter © 2011 Elsevier B.V. All rights reserved.
doi:10.1016/j.mee.2011.11.012

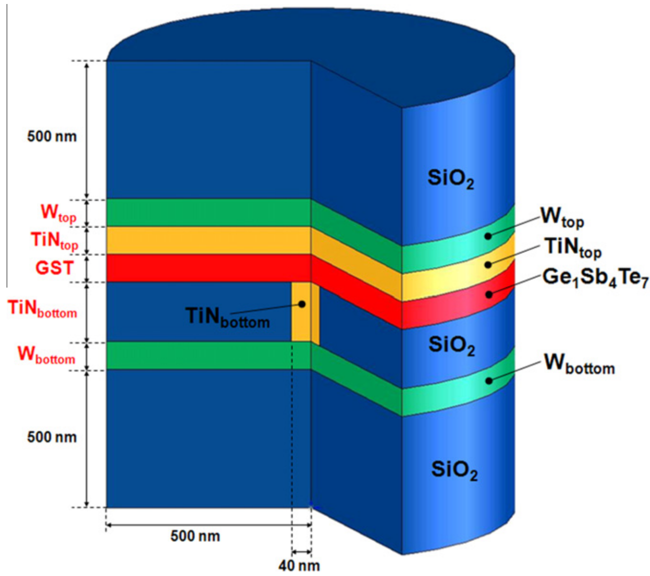

Fig. 1. Schematic of phase-change memory cell for simulations.

PCM cell since the various geometrical factors may inter-influence each other on heat transfer behavior.

Here, we report the thermal design of T-structured PCM cell with a contact diameter of 80 nm, which is a typical dimension for a conventional PCM cell [7–10]. Performance of the cell is evaluated in terms of the maximum cell temperature at 20 ns during the reset process as the process exhibits most extreme operating conditions in electrical as well as thermal aspects. Design variables consist of thicknesses of five constituting layers, i.e., top metal contact layer (TiN), top metal electrode layer (W), bottom metal contact layer (TiN), bottom metal electrode layer (W), and phase-change layer ($Ge_1Sb_4Te_7$). We correlate the simultaneous dependence of the maximum cell temperature on the thickness of five constituting layers into a single equation using advanced response surface method, or α-RSM, an advanced form of the conventional response surface method, to examine the multi-variable dependence on cell temperature evolution.

2. Methodologies

2.1. Numerical simulation

Fig. 1 shows a schematic of the PCM cell used in this study. A conventional T-structured cell with a contact diameter of 80 nm is employed. The phase-change layer is sandwiched between the top and the bottom electrodes of TiN and W. Joule heating is given by reset current of 0.4 mA which is applied between the top and the bottom W electrodes based on the following transient electro-thermal conduction equation;

$$K \cdot \nabla^2 T + \rho_e \cdot J^2 = \rho_d \cdot C_p \cdot \frac{\partial T}{\partial t} \qquad (1)$$

where T is temperature, k is thermal conductivity, J is current density, ρ_e is electrical resistivity, ρ_d is density, C_p is specific heat, and t is time. Numerical calculations are conducted using a commercial multiphysics solver CFD-ACE+ [14]. Quarter modeling is employed for simpler and faster calculations.

Volumetric properties are presented in Table 1. $Ge_1Sb_4Te_7$ (GST) is selected as the phase-change material since GST shows the fastest operating performance among GeSbTe ternary materials due to its low phase-change temperature as well as activation energy [15,16]. In-house measured thermal conductivity [17], electrical resistivity [18], and density [19] of GST are used whereas specific heat is adopted from the $Ge_2Sb_2Te_5$ value [8]. Based on Debye-approximated specific heat [20], the specific heat of $Ge_1Sb_4Te_7$ can be substituted by that of $Ge_2Sb_2Te_5$ due to similar phonon velocity and atomic number density [17]. Since we conduct studies on the reset process, we employ (poly)crystalline GST properties. Volumetric properties of other materials (W, TiN, and SiO_2) are adopted from other references [8,9].

We also consider the thermal boundary resistance since the effect of the thermal boundary resistance on the evolution of cell temperature is known to be extremely critical [21]. As the surface-to-volume ratio increases with decreasing feature size down to submicron regime, surface plays considerable role in heat transport behavior. Therefore, the thermal boundary resistance must be considered to achieve accurate simulation results [21]. We apply thermal boundary resistance along the boundaries of the phase-change layer since heat diffusion predominantly takes place inside the phase-change layer. Thermal boundary resistance values are set as follows; thermal boundary resistance between GST and TiN, $R_{GST-TiN} = 6.25 \times 10^{-8}$ m^2 K W^{-1}; and thermal boundary resistance between GST and SiO_2, $R_{GST-SiO_2} = 0.7 \times 10^{-8}$ m^2 K W^{-1} [22].

2.2. Correlations: advanced response surface method (α-RSM)

In methodological aspect, optimization is defined as a pursuit of assigned design variables that satisfy maximum or minimum (optimal) objective value under given design constraints. Prior to obtaining the optimal design variables, one must correlate the experimental (or analytical) results into a single equation. We employ such correlation scheme from the well-defined optimization process, in detail, α-RSM.

The design variables are thicknesses, t, of the five constituting layers from Fig. 1, which are two W layers (W_{top}, W_{bot}), two TiN layers (TiN_{top}, TiN_{bot}), and one phase-change layer (GST). The contact size is set a constant because the contact size is generally regarded as a parameter that is always favorable when reduced, and thus the value is determined by the state-of-the-art fabrication technology. Therefore, to give a feasible optimization process and results, we set the optimization variables as the thicknesses of five constituting layers, which can be easily achieved with current conventional fabrication technologies. Therefore, the design range is determined based on practically fabricable conditions; from 20 nm to 500 nm for $t_{TiN_{top}}$, $t_{TiN_{bot}}$, $t_{W_{top}}$, and $t_{W_{bot}}$; and from 20 nm to 200 nm for t_{GST}. Also, the objective value (or objective function) is defined as a maximum cell temperature at 20 ns during reset

Table 1
Physical properties of constituting materials.

Material	Thermal conductivity (W m^{-1} K^{-1})	Electrical resistivity (Ω m)	Density (kg m^{-3})	Specific heat (J kg^{-1} K^{-1})
$Ge_1Sb_4Te_7$ [a]	0.49 [17]	3.47×10^{-4} [18]	5685 [19]	193.55 [b] [8]
TiN [8]	29	1×10^{-6}	5400	599.07
W [8]	178	1.75×10^{-7}	19,300	133.68
SiO_2 [8]	1.1	1×10^{16}	2330	1330.47

[a] (Poly)crystalline phase.
[b] $Ge_2Sb_2Te_5$.

process as the cell temperature is a major indicator of the output performance of PCM cell.

To correlate, we employ α-RSM, which is an advanced form of the conventional response surface method. As mentioned earlier, optimization is based on a correlation function between actual values and response values. Conventional response surface method normally approximates the correlation function as a full quadratic equation as follows [23]:

$$y = C_0 + \sum_{i=1}^{k} C_i x_i + \sum \sum_{i<j=2}^{k} C_{ij} x_i x_j + \sum_{i=1}^{k} C_{ii} x_i^2 + \varepsilon \quad (2)$$

where y is objective function, x is design variable, k is number of design variables, C is coefficient, and ε is random error. It often may not be feasible to employ the conventional response surface method when dealing with broad design ranges and/or complex nonlinear phenomena as the quadratic equation cannot effectively follow the actual broad and/or complex results.

Therefore, to deal with such shortcomings, α-RSM introduces functional variables into the objective function [24,25] as follows:

$$y = C_0 + \sum_{i=1}^{k} C_i f(x_i) + \sum \sum_{i<j=2}^{k} C_{ij} f(x_i) f(x_j) + \sum_{i=1}^{k} C_{ii} f\left(x_i^2\right) + \varepsilon \quad (3)$$

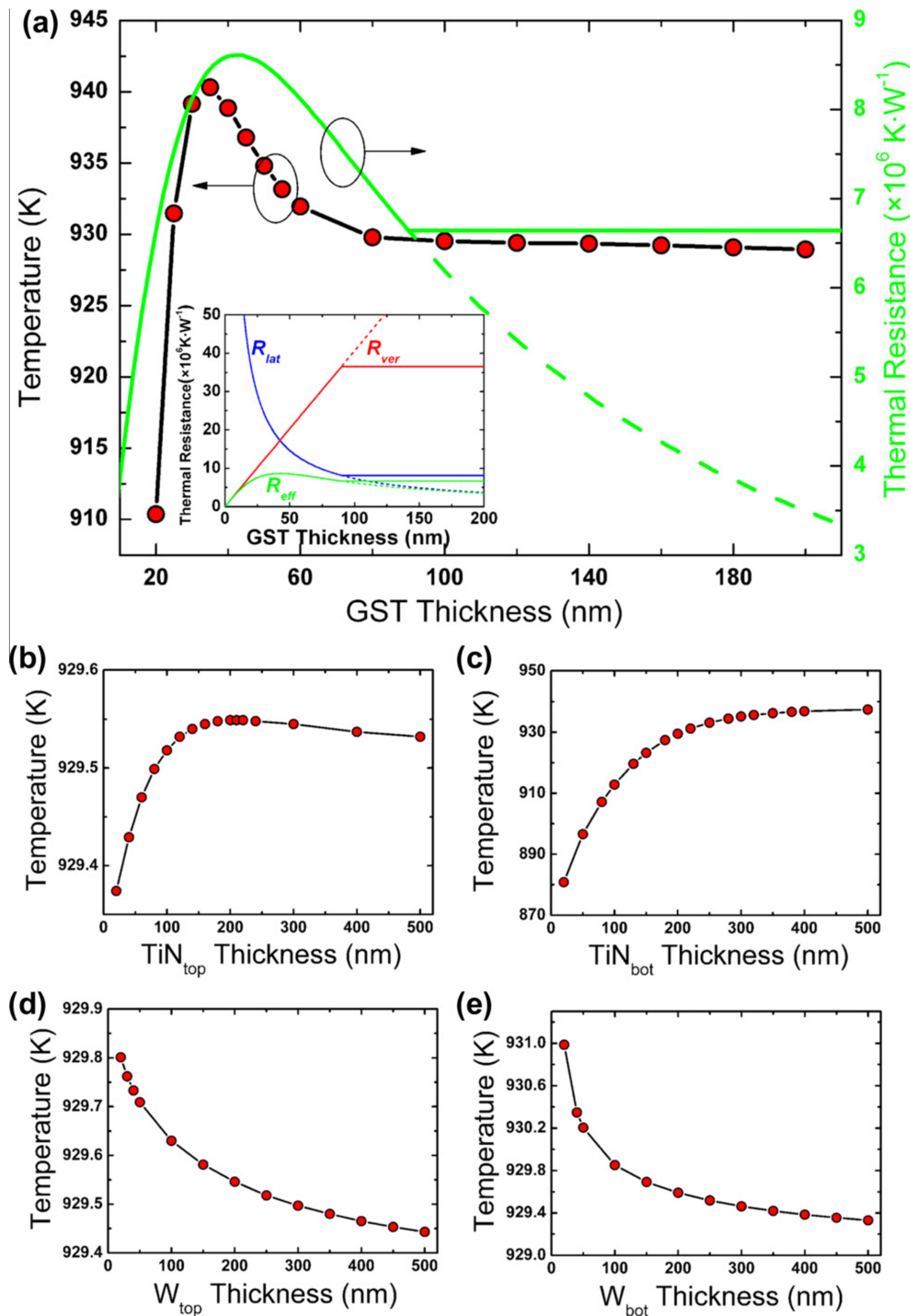

Fig. 2. Parametric studies on each variable: (a) GST; (b) TiN_{top}; (c) TiN_{bot}; (d) W_{top}; and (e) W_{bot}. Behavior of a single variable is analyzed while setting the other variables as constants; t_{GST} = 100 nm, $t_{TiN_{top}} = 100$ nm, $t_{TiN_{bot}} = 200$ nm, $t_{W_{top}} = 250$ nm, and $t_{W_{bot}} = 250$ nm. In (a), the green solid line indicates effective thermal resistance regarding finite lateral thermal diffusion in the GST layer whereas the green dashed line indicate effective thermal resistance regarding infinite lateral thermal diffusion in the GST layer. Inset indicates plot of Eq. (4). Solid lines imply finite lateral thermal diffusion in the GST layer whereas dashed lines imply infinite lateral thermal diffusion in the GST layer. (For interpretation of the references to color in this figure legend, the reader is referred to the web version of this article.)

The main idea of introducing functional variable is that there exist certain functional correlations between a variable and the objective function due to their own intrinsic physical behavior. By doing this, one obtains a more accurate response surface equation with broader design range. Functions in the form of x_i^n, $\log(x_i)$, $\sin(x_i)$, $\exp(x_i)$, etc. can be employed. Detailed procedures of α-RSM can be found from our previous works [24–26].

3. Results and discussion

To understand the influence of designated variables on the maximum cell temperature, we conduct parametric studies on each variable while setting other variables as constants; t_{GST} = 100 nm, $t_{TiN_{top}} = 100$ nm, $t_{TiN_{bot}} = 200$ nm, $t_{W_{top}} = 250$ nm, and $t_{W_{bot}} = 250$ nm. The results are presented in Fig. 2. As can be seen from Fig. 2(a), the maximum cell temperature dependence on GST thickness is non-monotonic, but a certain thickness value exists for the maximum cell temperature to occur. This can be explained in terms of the effective thermal resistance of the GST layer. By assuming that the heat mainly flows through cross-plane and radial directions, the effective thermal resistance of the GST layer can be described in terms of parallel connection between lateral thermal resistance and vertical (upward) thermal resistance. Heat flow through downward direction can be ignored due to finite thermal boundary resistance. Thermal crosstalk between lateral heat flows is also neglected since it is minimal. We can calculate the effective thermal resistance of GST as follows:

$$R_{eff} = \left(R_{lat}^{-1} + R_{ver}^{-1}\right) = \left(\left(L_{GST}/k_{GST}\cdot(t_{GST}\cdot 2\pi r_{ct})\right)^{-1} + \left(t_{GST}/k_{GST}\cdot(\pi r_{ct}^2)\right)^{-1}\right)^{-1} \quad (4)$$

where R_{lat} is lateral thermal resistance, R_{ver} is vertical thermal resistance, k_{GST} is thermal conductivity of GST (0.49 W m^{-1} K^{-1}), L_{GST} is lateral GST length, and r_{ct} is contact radius (40 nm). Here, L_{GST} is set as thermal diffusion length ($\sqrt{\alpha\cdot\tau}\sim 90$ nm where $\alpha = 0.4\times 10^{-6}$ m^2 s^{-1} is thermal diffusivity of GST and τ = 20 ns is thermal diffusion time) since this is an unsteady heat conduction problem and thereby heat diffuses in limited distance. Plot of Eq. (4) is presented in the inset of Fig. 2(a).

As the parallel thermal connection is calculated based on Matthiessen's rule, where the smallest thermal resistance dominates the total effective thermal resistance, the dominant heat flows through the lowest thermal resistance direction. In thin GST region (<40 nm), as t_{GST} increases, the vertical thermal resistance increases whereas the lateral thermal resistance decrease; however, still the vertical thermal resistance dominates the overall thermal resistance. As t_{GST} reaches about 40 nm, the lateral thermal resistance becomes smaller than the vertical thermal resistance and the dominant thermal resistance is reversed. Therefore, although the vertical thermal resistance increases with t_{GST}, the dominant lateral thermal resistance decreases, resulting decrease of the effective thermal resistance and eventually temperature decrease. As t_{GST} further increases, the actual simulated result tends to level off around 90 nm while the effective thermal resistance, Eq. (4), continuously decreases. As mentioned earlier, because this is an unsteady heat conduction condition, heat diffuses in a limited distance of about 90 nm. This can be also applied in vertical direction of the GST layer. In other words, the vertical heat diffusion is also limited by the thermal diffusion length. Therefore, to give more realistic conditions, we set a constant value of 90 nm for t_{GST} when it exceeds 90 nm. The results show that this approximation follows much better than the simulated results (green solid line in Fig. 2(a)). Discrepancy of the peak value between numerical results (35 nm) and Eq. (4) (40 nm) may be attributed to the thermal mass and the resistance of other constituting layers in the vicinity of the GST layer.

Temperature behaviors of TiN_{top}, W_{top}, and W_{bot} layers can also be explained with an effective thermal resistance concept. However, due to the varying length scales that the each layer possesses, peak value shifts even to the outside the given design range, and W_{top} and W_{bot} layers show rather monotonic decrease with increasing thicknesses under the design range. This will be discussed later in detail.

Meanwhile, the maximum cell temperature increases with $t_{TiN_{bot}}$ (Fig. 2(c)). This is additionally attributed to the laterally confined heat flow. TiN_{bot} layer is shaped like a narrow cylinder with a diameter of 80 nm and is surrounded by a SiO_2 layer which is a thermal insulator. Therefore, the lateral thermal resistance should significantly increase compared to other layers, thereby making vertical thermal resistance a dominant factor in determining the effective thermal resistance. In conjunction with the inset of Fig. 2(a), the vertical thermal resistance increases with layer thickness, resulting maximum cell temperature increase with layer thickness.

To find out an optimal configuration that exhibits maximum cell temperature and suggest thermal design guidelines in designing the PCM cell, we employ α-RSM as a means to correlate all five variables into a single equation. From Fig. 2, under a given design range, one would naively determine that the maximum cell temperature occurs when t_{GST} = 35 nm, $t_{TiN_{top}} = 210$ nm, $t_{TiN_{bot}} = 500$ nm, $t_{W_{top}} = 20$ nm, and $t_{W_{bot}} = 20$ nm. However, from the results obtained by α-RSM, we find a somewhat different thickness configuration which will be explained in the following.

As mentioned in the previous section, to employ α-RSM, functional behavior of participating variables must be known prior to correlation. This task can be done using the parametric study results from Fig. 2. By curve-fitting the results with different kinds of functional domains, we determine that the objective functions of W_{top}, W_{bot}, TiN_{bot}, and GST show better fit to log functions whereas the objective function for TiN_{top} fits the best in its original form. These functional variables are applied to Eq. (3) for a correlation of 40 individual simulation sets that are selectively chosen using D-optimal method [27]. The response surface equation obtained is as follows:

$$\begin{aligned} T_{max} = & -51.22 - 0.711\cdot\log(x_1) + 0.589\cdot\log(x_2) + 0.009\cdot x_3 \\ & + 58.27\cdot\log(x_4) + 1166.5\cdot\log(x_5) + 1.043\cdot\log(x_1) \\ & \cdot\log(x_2) + 0.007\cdot\log(x_1)\cdot x_3 - 5.49\cdot\log(x_1)\cdot\log(x_4) \\ & + 6.794\cdot\log(x_1)\cdot\log(x_5) - 0.0088\cdot\log(x_2)\cdot x_3 \\ & + 1.724\cdot\log(x_2)\cdot\log(x_4) - 3.033\cdot\log(x_2)\cdot\log(x_5) \\ & - 0.0034\cdot x_3\cdot\log(x_4) - 0.0036\cdot x_3\cdot\log(x_5) + 40.18 \\ & \cdot\log(x_4)\cdot\log(x_5) + 0.3043\cdot\log^2(x_1) - 0.085\cdot\log^2(x_2) \\ & + 5.9\times 10^{-6}\cdot x_3^2 - 20.56\cdot\log^2(x_4) - 408.22\cdot\log^2(x_5) \end{aligned} \quad (5)$$

where x_1 is $t_{W_{top}}$, x_2 is $t_{W_{bot}}$, x_3 is $t_{TiN_{top}}$, x_4 is $t_{TiN_{bot}}$, and x_5 is t_{GST}. The coefficient of each term represents the degree of influence on the objective function (or the maximum cell temperature). One can easily predict that t_{GST} and $t_{TiN_{bot}}$ will be the most dependent factors on the objective function. This equation does not imply any physical meaning, but is the most accurate full quadratic equation to be fitted on the actual 40 simulation results. We apply this equation to additional simulations of more than 200 sets for verification. It can be seen from Fig. 3 that the response surface follows excellent to the actual simulation results within 0.3% of error. R^2 and adjusted R^2 values are calculated to be 0.978 and 0.976, respectively, which again represents the excellence of optimized results.

This equation can be a powerful tool in designing the PCM cell since this equation represents a performance map of the assigned variables. Given design ranges and constraints, one can easily plot a map regarding variables of one's interest. Additionally, one can

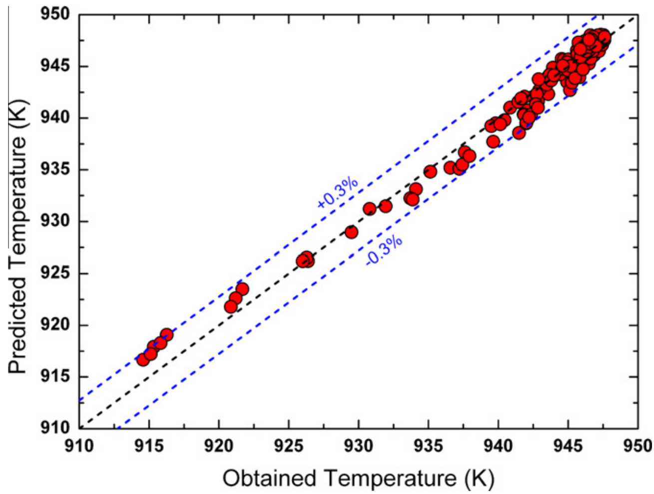

Fig. 3. Comparison between calculated and predicted maximum temperatures.

ultimately find an optimal configuration that contributes to the maximum performance. This is presented later in detail.

Utilizing the optimization technique to Eq. (5), we obtain the optimal configuration of the design variables which exhibits maximum performance. The optimal values obtained for the variables from Eq. (5) are as follows; t_{GST} = 36 nm, $t_{TiN_{top}} = 20$ nm, $t_{TiN_{bot}} =$ 500 nm, $t_{W_{top}} = 20$ nm, and $t_{W_{bot}} = 20$ nm. By substituting such values into Eq. (5), the predicted maximum temperature is 948.07 K. Fig. 4 shows simulated temperature and current density distributions of the optimized cell at 20 ns. The maximum cell temperature reaches up to 947.6 K in 20 ns, showing average and peak temperature rise rate of 4.7×10^{10} K s^{-1} and 33.2×10^{10} K s^{-1}, respectively, with a maximum Joule heating rate of 1.65×10^{15} W m^{-3} (or a maximum current density of 1.52×10^{11} A m^{-2}).

To verify the optimized results, we again conduct parametric studies on the optimized results by setting all variables constant to the optimized results except for the certain variable, which will be parametrically analyzed. Fig. 5 shows parametric studies of each variable with other variables being constant values of the optimized results. The blue dashed line represents the predicted optimal values. Results show that the predicted optimal values are well proved to be the maximum output that the device can perform in the given optimization range.

It is interesting to know that the behavior of TiN_{top} (Fig. 5(b)) is somewhat different from prior parametric study (Fig. 2(b)). In detail, the maximum cell temperature occurs at a certain value of $t_{TiN_{top}} = 210$ nm in Fig. 2 whereas another maximum cell temperature occurs at the lower limit ($t_{TiN_{top}} = 20$ nm). This is attributed to the coupled interaction between the thicknesses of GST and TiN_{top} layer on the maximum cell temperature. When the GST layer becomes thicker, heat spreading inside the GST layer becomes more significant. The heated area on the bottom surface of the TiN_{top} layer is increased in proportion to GST thickness. This makes TiN_{top}

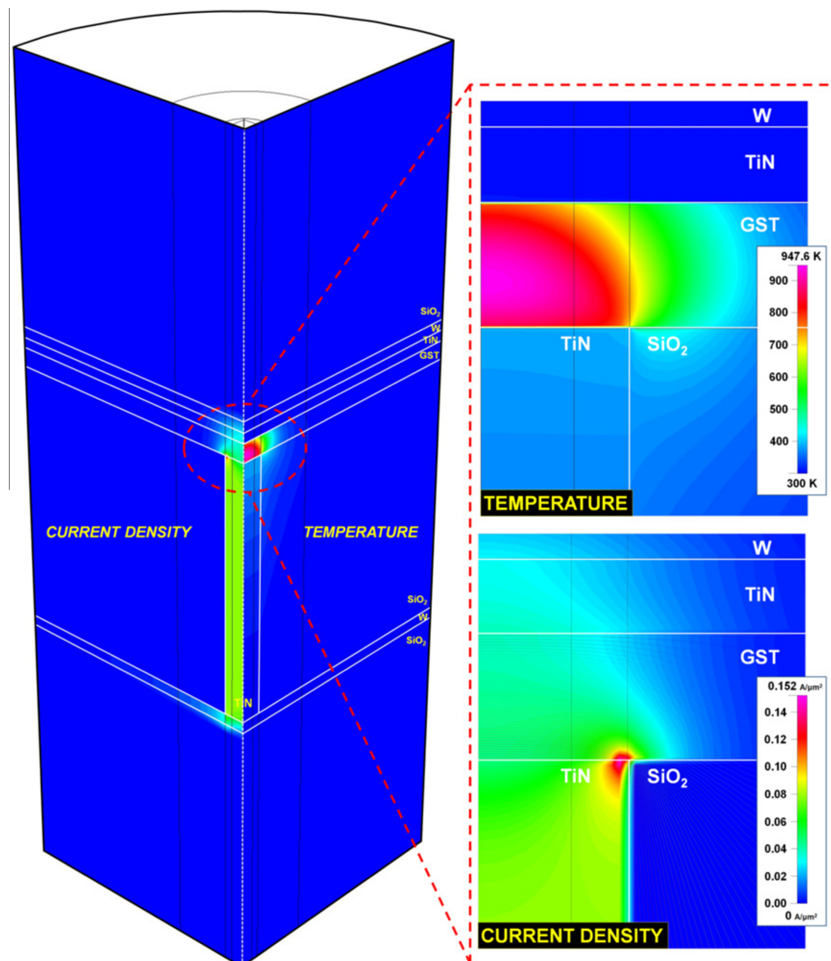

Fig. 4. Temperature and current density distributions of an optimized cell at 20 ns during reset process.

layer less sensitive to lateral heat diffusion, resulting vertical heat flow dominant. Such modified thermal resistance of TiN_{top} can be expressed as follows:

$$R_{ver} = \frac{t_{TiN_{top}}}{k_{TiN} \cdot \pi (r_{ct} + t_{GST})^2} \quad (6)$$

$$R_{lat} = \frac{\sqrt{\alpha_{TiN} \cdot (\tau - (t_{GST}^2/\alpha_{GST}) - \varepsilon_{tbr})}}{k_{TiN} \cdot 2\pi (r_{ct} + t_{GST}) \cdot t_{TiN_{top}}} \quad (7)$$

where k_{TiN} is thermal conductivity of TiN (29 W m^{-1} K^{-1}), α_{TiN} is thermal diffusivity of TiN (8.96×10^{-6} m^2 s^{-1}), α_{GST} is thermal diffusivity of GST (0.41×10^{-6} m^2 s^{-1}), and ε_{tbr} is a compensation term for thermal boundary resistance.

From these equations, when the GST layer is significantly thick (~thermal diffusion length), it is known that the thermal diffusion length inside the TiN_{top} layer decreases dramatically as the thermal diffusion length inside the TiN_{top} layer follows a function of $f(t_{GST}) \sim \sqrt{1 - c \cdot t_{GST}^2}$ where c is a constant that will eventually lead to sudden decreased lateral thermal resistance.

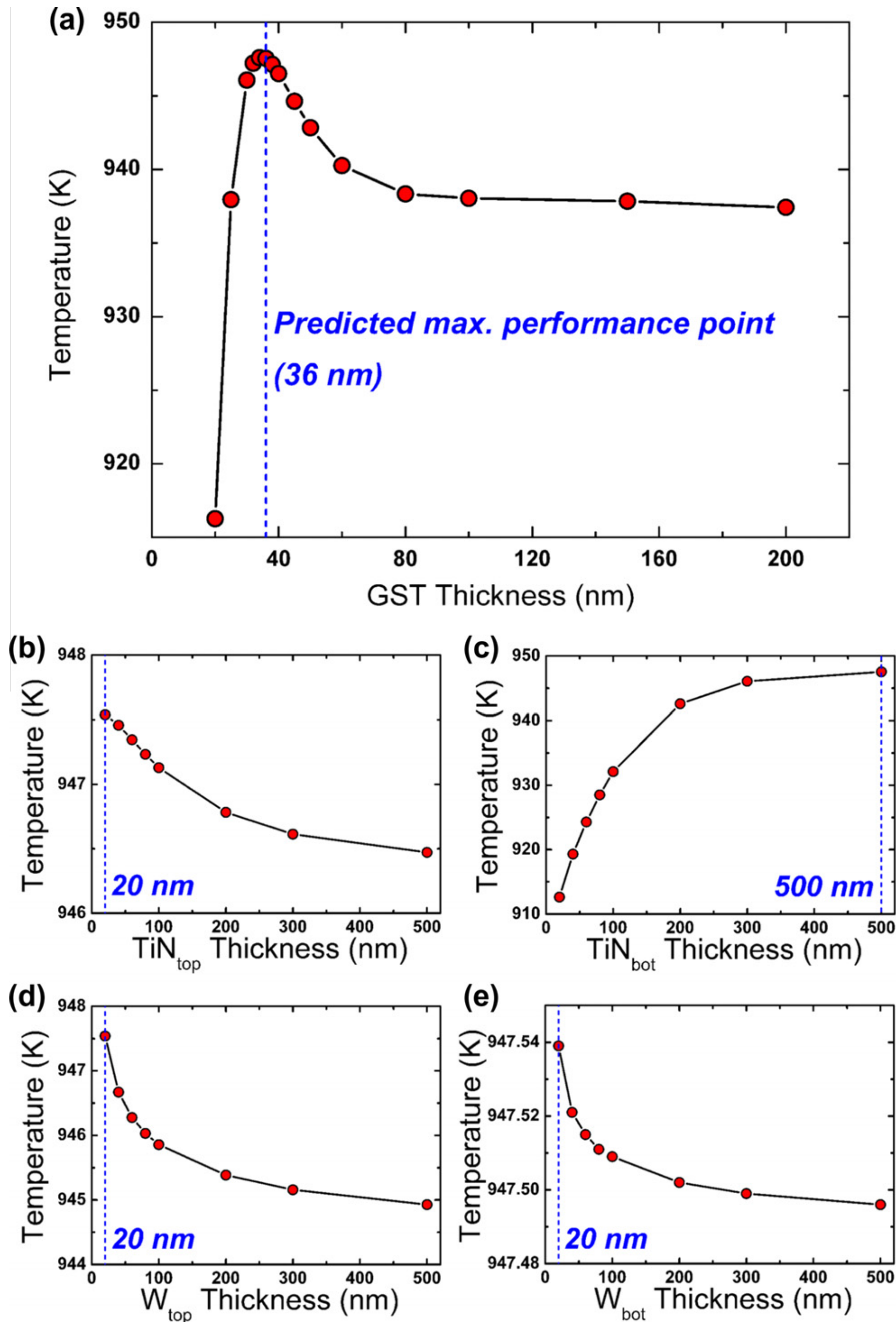

-22-

Fig. 5. Validation of predicted optimal values: (a) GST; (b) TiN_{top}; (c) TiN_{bot}; (d) W_{top}; and (e) W_{bot}. Blue dashed lines represent predicted optimal values obtained by α-RSM. (For interpretation of the references to color in this figure legend, the reader is referred to the web version of this article.)

Fig. 6(a) shows plot of Eqs. (6) and (7) as functions of t_{GST} when $t_{TiN_{top}}$ is 50 nm. As predicted, when GST is thin, the vertical thermal resistance is smaller than the lateral thermal resistance. Meanwhile, as GST becomes thicker, the lateral thermal resistance dramatically decreases, thereby dominating the overall effective thermal resistance of the TiN_{top} layer. Simulation results considering such effects are presented in Fig. 6(b) where the peak temperature shift is clearly shown.

The presented results are only a limited case of coupled interaction between the constituting layers. Regarding that the TiN_{top} layer in Fig. 2(b) shows the maximum cell temperature at around 210 nm when t_{GST} is 100 nm, other layers besides GST may unambiguously influence the performance behavior of the TiN_{top} layer which again emphasizes the importance of multi-variable thermal analysis in designing the PCM cells.

Fig. 7 shows two specific cases on resultant maps of objective function, i.e. maximum cell temperature, as functions of two different variables that are deduced from Eq. (5). In detail, Fig. 7(a) presents a resultant map as a function of $t_{TiN_{top}}$ and $t_{TiN_{bot}}$ when $t_{W_{top}} = 20$ nm, $t_{W_{bot}} = 20$ nm, and $t_{GST} = 36$ nm, and Fig. 7(b) presents a resultant map as a function of t_{GST} and $t_{TiN_{bot}}$ when $t_{W_{top}} = 20$ nm, $t_{W_{bot}} = 20$ nm, and $t_{TiN_{bot}} = 20$ nm. Using these resultant maps, one can easily understand the behavior of multi-variable dependence of the objective function, i.e. maximum temperature, and obtain the optimal value directly. Moreover, when design constraints are given, this can be employed directly in designing the PCM cell with minimal effort. For example, one can select any thickness of the TiN_{top} layer under the given design range (20–500 nm) for designing the best-performing device when the design range of $t_{TiN_{bot}}$ is constrained by having less than 200 nm as $t_{TiN_{top}}$ is insensitive to the output performance when $t_{TiN_{bot}}$ is thinner than 200 nm. This implies that the thickness of the TiN_{top} layer is not a dominant factor when designing the PCM cell in such a specific case.

It should be noted that there exists a certain reset power which results in a maximum output performance (or cell temperature). Fig. 8 shows the maximum cell temperature as a function of reset power for over 200 different shapes of PCM cells. Since 20 ns is a temporal scale to be electrically steady whereas thermally unsteady, just by increasing the power will not result in increase of the maximum cell temperature. Therefore, thermal analysis/design is critical and thermal optimization should once again be emphasized in designing the PCM cell. Moreover, in order to investigate the cell behavior deeply enough to achieve the maximum cell performance as much as possible, several other factors such as the contact size and reset time may also be considered. Especially, the contact size is directly related to the reset current and power consumption of the device, and owing to the excellent scalability of the PCM cells,

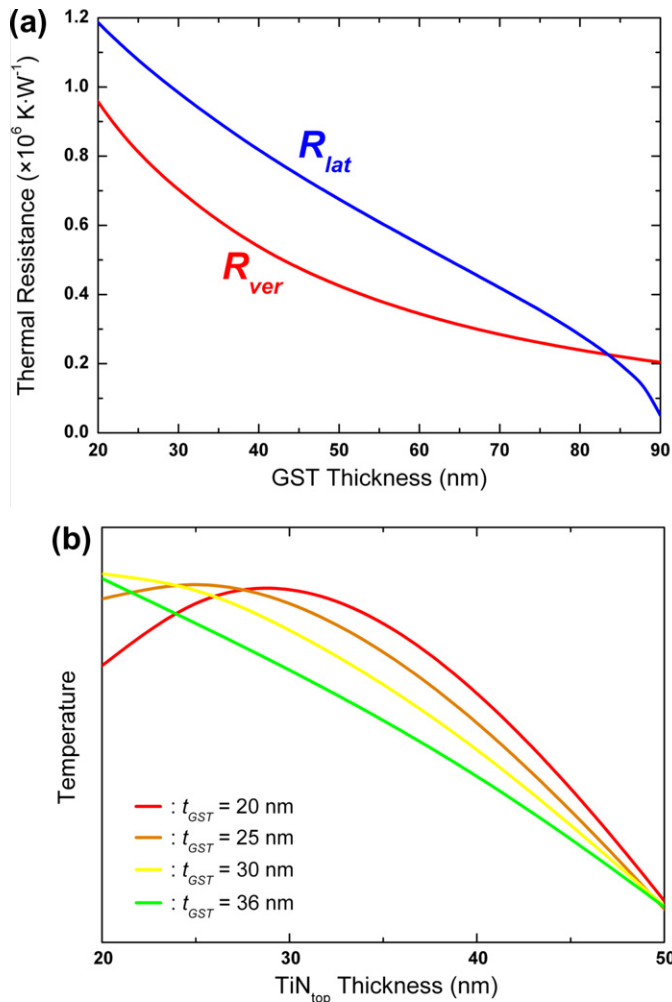

Fig. 6. Influence of GST layer thickness on TiN_{top}. (a) Plot of Eq. (6) and Eq. (7) as functions of t_{GST} when $t_{TiN_{top}} = 50$ nm. (b) Simulated results on maximum cell temperature as functions of $t_{TiN_{top}}$ when $t_{TiN_{bot}} = 200$ nm, $t_{W_{top}} = 250$ nm, and $t_{W_{bot}} = 250$ nm. t_{GST}-dependent peak shift is clearly shown. Temperature scales are adjusted for clear observation.

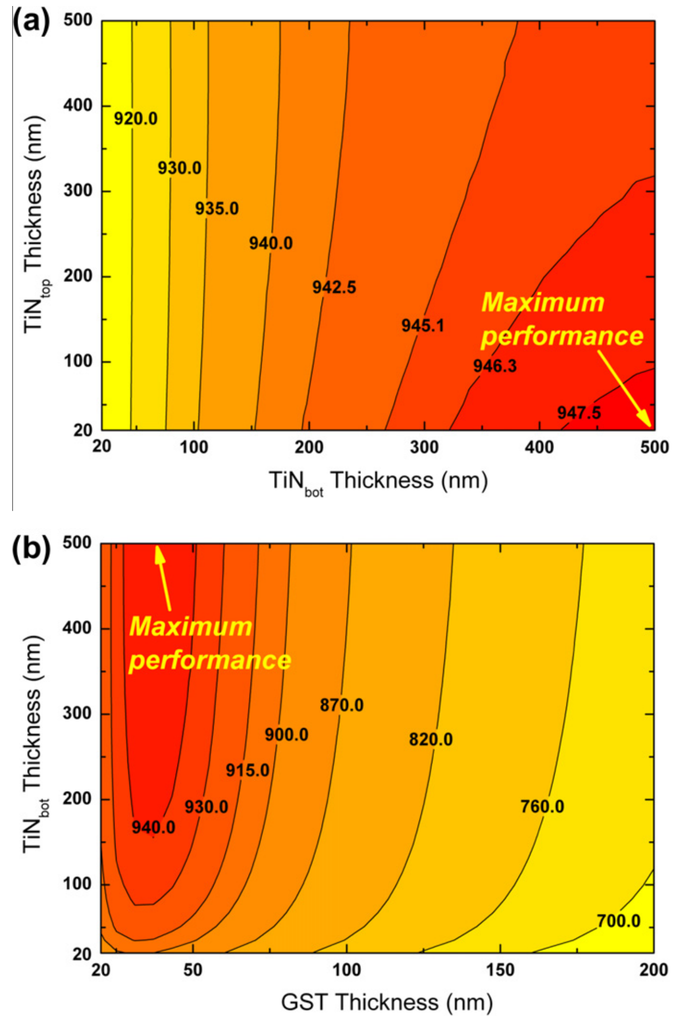

Fig. 7. Resultant maps for multi-variable behavior on maximum cell temperature; (a) TiN_{top} vs. TiN_{bot} when GST = 36 nm, W_{top} = 20 nm, and W_{bot} = 20 nm; (b) GST vs. TiN_{bot} when TiN_{top} = 20 nm, W_{top} = 20 nm, and W_{bot} = 20 nm.

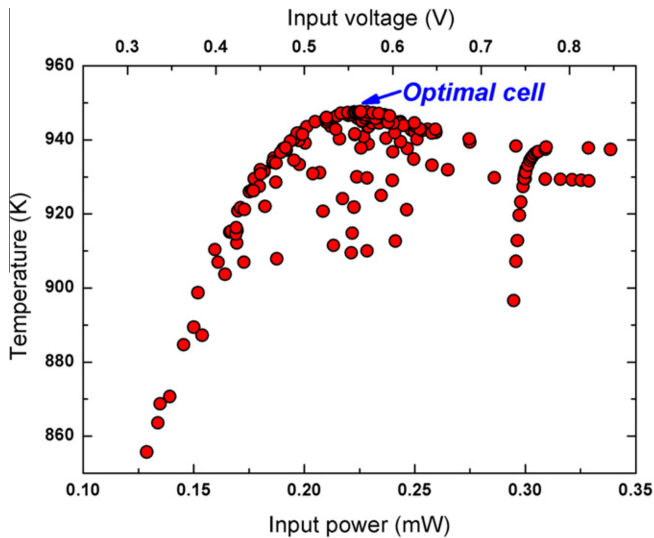

Fig. 8. Maximum cell temperature vs. input power. Input power is calculated based on multiplication of input current (0.4 mA) and voltage difference between two W electrodes. The corresponding voltage difference is also plotted for comparison.

the contact size is a parameter that is always favorable when reduced. Therefore, additional studies regarding contact width and length should be investigated in the future studies.

4. Conclusion

We have conducted the thermal design and analysis of T-structured phase-change memory cell with a contact diameter of 80 nm using an advanced response surface method. Device performance was evaluated in terms of the maximum cell temperature at 20 ns during the reset process. Design variables consisted of thicknesses of five constituting layers under the given design ranges. Simulated results of the five individual variables were correlated simultaneously using α-RSM within 0.3% error. The results showed that the output performance was maximum when the two top metal layers and the bottom metal electrode layer became thinner whereas the bottom metal contact layer became thicker. Meanwhile, there existed a certain phase-change layer thickness, which was 36 nm in this study, for maximum output performance. These results were caused by the limited thermal diffusion length as well as the thermal interaction among the constituting layers. We conclude that the multi-variable thermal analysis and design can lead to deeper understanding of underlying heat transfer phenomena in PCM cells and thereby design of better-performing devices.

References

[1] M.H.R. Lankhorst, B.W.S.M.M. Ketelaars, R.A.M. Wolters, Nature Mater. 4 (2005) 347–352.
[2] M. Wuttig, N. Yamada, Nature Mater. 6 (2007) 824–832.
[3] S. Raoux, R.M. Shelby, J. Jordan-Sweet, B. Munoz, M. Salinga, Y.-C. Chen, Y.-H. Shih, E.-K. Lai, M.-H. Lee, Microelectron. Eng. 85 (2008) 2330–2333;
A.L. Lacaita, D. Ielmini, D. Mantegazza, Solid-State Electron. 52 (2008) 1443–1451.
[4] A.L. Lacaita, Solid-State Electron. 50 (2006) 24–31.
[5] Y. Li, C.-H. Hwang, T.-Y. Li, H.-W. Cheng, Nanotechnology 20 (2009) 285701.
[6] S.B. Kim, H.-S.P. Wong, IEEE Electron. Dev. Lett. 28 (2007) 697–699.
[7] Y. Yin, H. Sone, S. Hosaka, Jpn. J. Appl. Phys. 45 (2006) 6177–6181.
[8] S.S. Kim, S.M. Jeong, K.H. Lee, Y.K. Park, Y.T. Kim, J.T. Kong, H.L. Lee, Jpn. J. Appl. Phys. 44 (2005) 5943–5948.
[9] Y.T. Kim, K.-H. Lee, W.-Y. Chung, T.-K. Kim, Y.-K. Park, J.-T. Kong, in: Proc. Int. Conf. SISPAD 2003, pp. 211–214.
[10] A. Pirovano, F. Pellizzer, I. Tortorelli, A. Riganó, R. Harrigan, M. Magistretti, P. Petruzza, E. Varesi, A. Redaelli, D. Erbetta, T. Marangon, F. Bedeschi, R. Fackenthal, G. Atwood, R. Bez, Solid-State Electron. 52 (2008) 1467–1472.
[11] A. Pirovano, F. Pellizzer, A. Redaelli, I. Tortorelli, E. Varesi, F. Ottogalli, M. Tosi, P. Besana, R. Cecchini, R. Piva, M. Magistretti, M. Scaravaggi, G. Mazzone, P. Petruzza, F. Bedeschi, T. Marangon, A. Modelli, D. Ielmini, A.L. Lacaita, R. Bez, in: Proc. ESSDERC 2005, pp. 313–316.
[12] U. Russo, D. Ielmini, A. Redaelli, A.L. Lacaita, IEEE Trans. Electron. Dev. 55 (2008) 506–514.
[13] J.B. Philipp, B. Ruf, C. Ruster, D. Andres, P. Majewski, M. Kund, T.D. Happ, R. Bergmann, in: Proc. NVMTS 2008, pp. 1–3.
[14] CFD-ACE+ User Manual, Version 2008.0, ESI-Group, 2008.
[15] N. Yamada, E. Ohno E, K. Nishiuchi, N. Akahira, M. Takao, J. Appl. Phys. 69 (1991) 2849–2856.
[16] E. Morales-Sánchez, E.F. Prokhorov, J. González-Hernández, A. Mendoza-Galván, Thin Solid Films 471 (2005) 243–247.
[17] S. Shin, H.K. Kim, J. Song, D.J. Choi, H.H. Cho, J. Appl. Phys. 107 (2010) 033518.
[18] H.K. Kim, S.Y. Lee, D.J. Choi, S. Shin, H.H. Cho, J.S. Roh, J. Kor. Phys. Soc. 55 (2009) 1896–1900.
[19] S. Shin, K.M. Kim, J. Song, H.K. Kim, D.J. Choi, H.H. Cho, IEEE Trans. Electron. Dev. 58 (2011) 782–791.
[20] C.L. Tien, A. Majumdar, F.M. Gerner, Microscale Energy Transport, Taylor and Francis, Washington, DC, 1998.
[21] J.P. Reifenberg, D.L. Kencke, K.E. Goodson, IEEE Electron. Dev. Lett. 29 (2008) 1112–1114.
[22] R. Warren, J.P. Reifenberg, K.E. Goodson, in: Proc. ITHERM, 2008, pp. 1018–1045.
[23] R.H. Myers, D.C. Montgomery, Response Surface Methodology: Process and Product Optimization Using Designed Experiments, Wiley, New York, NY, 2002.
[24] K.M. Kim, H. Lee, B.S. Kim, S. Shin, D.H. Lee, H.H. Cho, Heat Mass Transf. 45 (2009) 1617–1625.
[25] K.M. Kim, B.S. Kim, D.H. Lee, H. Moon, H.H. Cho, Energy 35 (2010) 2400–2406.
[26] B.S. Kim, B.S. Kwak, S. Shin, S. Lee, K.M. Kim, H.-I. Jung, H.H. Cho, Int. J. Heat. Mass. Transf. 54 (2011) 118–125.
[27] M. Kaufman, V. Balabanov, S.L. Burgee, A.A. Giunta, B. Grossman, R.T. Haftka, W.H. Mason, L.T. Watson, Comput. Mech. 18 (1996) 112–126.